

Environmental Influence on Passive Films Formed on Alloy 22

*A.W. Szmodis, K.L. Anderson, J.C. Farmer, T. Lian,
C.A. Orme*

This article was submitted to
National Association of Corrosion Engineers International,
CORROSION/03 Conference
San Diego, CA
March 16-20, 2003

October 7, 2002

U.S. Department of Energy

Lawrence
Livermore
National
Laboratory

DISCLAIMER

This document was prepared as an account of work sponsored by an agency of the United States Government. Neither the United States Government nor the University of California nor any of their employees, makes any warranty, express or implied, or assumes any legal liability or responsibility for the accuracy, completeness, or usefulness of any information, apparatus, product, or process disclosed, or represents that its use would not infringe privately owned rights. Reference herein to any specific commercial product, process, or service by trade name, trademark, manufacturer, or otherwise, does not necessarily constitute or imply its endorsement, recommendation, or favoring by the United States Government or the University of California. The views and opinions of authors expressed herein do not necessarily state or reflect those of the United States Government or the University of California, and shall not be used for advertising or product endorsement purposes.

This is a preprint of a paper intended for publication in a journal or proceedings. Since changes may be made before publication, this preprint is made available with the understanding that it will not be cited or reproduced without the permission of the author.

This report has been reproduced directly from the best available copy.

Available electronically at <http://www.doc.gov/bridge>

Available for a processing fee to U.S. Department of Energy

And its contractors in paper from

U.S. Department of Energy

Office of Scientific and Technical Information

P.O. Box 62

Oak Ridge, TN 37831-0062

Telephone: (865) 576-8401

Facsimile: (865) 576-5728

E-mail: reports@adonis.osti.gov

Available for sale to the public from

U.S. Department of Commerce

National Technical Information Service

5285 Port Royal Road

Springfield, VA 22161

Telephone: (800) 553-6847

Facsimile: (703) 605-6900

E-mail: orders@ntis.fedworld.gov

Online ordering: <http://www.ntis.gov/ordering.htm>

OR

Lawrence Livermore National Laboratory

Technical Information Department's Digital Library

<http://www.llnl.gov/tid/Library.html>

Paper submitted for NACE International Annual Conference
March 16-20 2003, San Diego CA

TITLE: Environmental Influence on Passive Films Formed on Alloy 22
AUTHORS: Alan W. Szmodis, Kelly L. Anderson, Joseph C. Farmer, Tiangan Lian, and
Christine A. Orme, Lawrence Livermore National Laboratory, Livermore, CA

Contact Author:

Christine A. Orme
Lawrence Livermore National Laboratory
L-350
7000 East Ave
Livermore, CA 94550
USA

Email: Orme1@llnl.gov
Voice: (1)-925-423-9509
Fax: (1)-925-422-6892

Abstract

The passive corrosion rate of Alloy 22 is exceptionally low in a wide range of aqueous solutions, temperatures and electrochemical potentials. Alloy 22 contains approximately 22% chromium (Cr) by weight; thus, it forms a Cr-rich passive film in most environments. Very little is known about the composition, thickness and other properties of this passive film. The aim of this research was to determine the general characteristics of the oxide film that forms on Alloy 22, as a function of solution pH, temperature and applied electrochemical potential.

1. Introduction

Alloy 22 (UNS# N06022) is a nickel (Ni) based alloy with nominally 22% chromium (Cr), 13% molybdenum (Mo), 3% tungsten (W) and 3% iron (Fe) as shown in Table 1. It is amongst the most corrosion resistant engineering materials available today and is thus being considered as a barrier material for nuclear waste containment by the Yucca Mountain Program. The passive corrosion rate of Alloy 22 in a wide range of aqueous solutions, temperatures and electrochemical potentials is exceptionally low. The high chromium concentration present in Alloy 22 allows a Cr-rich passive film to form in most environments. Very little is known about the composition, thickness and other properties of this passive film. The corrosion characteristics are tested in a series of multi-component waters derived from the geochemistry of the Yucca Mountain Site. This work focuses on the characteristics of oxide films formed in a saline solution with pH 8.

Atomic force microscopy (AFM), scanning electron microscopy (SEM), and x-ray photoelectron spectroscopy (XPS) were used to characterize the transformation of the surface oxide as Alloy 22 was potentiodynamically driven from the passive region to transpassive dissolution. Atomic force microscope images show that as the voltage is increased the surface is changed from a thin passive oxide to a bilayer structure that

includes a thick (~300nm) porous overlayer. From x-ray photo-emission spectroscopy we show that the inner oxide layer is composed of chromium, nickel, iron, and molybdenum oxides whereas the outer layer is predominately iron and nickel oxide. We show that the pore structures and film thickness can be tuned using electrochemical parameters such as temperature and voltage.

2. Methods

A saturated Ag/AgCl reference electrode, platinum counter electrode and an Alloy 22 working electrode were used in a three-electrode configuration with a commercial potentiostat for all of the electrochemical measurements. The reference electrode and a condenser were jacketed and cooled using chilled, flowing water. A lugin probe filled with test solution was used to complete the salt bridge. The solutions were either de-aerated with N₂ gas or aerated with filtered laboratory air for ~ 1 hour prior to the start of the experiment. A flow of 100 sccm was maintained throughout the duration of the experiment. The open circuit potential was monitored for approximately one hour prior to either potentiodynamic or potentiostatic scans. Potentiodynamic scans were ramped at a rate of 0.167V/s (600mv/hour). The cell was filled with 900ml of test solution and emplaced in a silicon oil bath maintained at temperature (90C). The solution temperature was checked at the beginning and end of the experiment.

Sample and sample holder

The samples were 5/8" diameter disks laser cut from 1/4" rolled plate of Alloy 22. One side was polished in stages using 5-micron diamond paste, 1-micron diamond paste, and 0.02-micron colloidal silica on low nap clothes. The samples were polished in a batch (and not always re-polished immediately prior to the electrochemistry experiments) and thus the initial starting surface had varying thicknesses of oxide films resulting from varying length of exposure to laboratory air under ambient conditions. The backs were stamped for identification purposes. The sample holder design was based on ASTM G5 with the pieces exposed to solution made of PVP which is less deformable than Teflon. A Teflon washer seals the sample in the sample holder leaving ~0.7cm² surface area exposed to the solution. The exposed area is measured for each sample.

Solution setup

Aqueous solutions were designed based on well waters (J-13) obtained from near the Yucca Mountain site. Three solutions were designed: one acidic, one near neutral and the other basic, to represent the range of potential environments the outer metal barrier could be exposed to. The solution used in this study is a ten times concentrated version of the near neutral solution, named "simulated concentrated water" (SCW). The composition is provided in table 2. The main features of SCW are that it is a carbonate containing, pH 8, high ionic strength (I~2.8 M) solution with Cl⁻/NO₃⁻ ratio near one.

Analysis Techniques (AFM, SEM, XPS)

Atomic force microscopy was used to obtain the surface morphology of dry samples both before and after electrochemical modification. Imaging was performed using Digital Instruments 3100 and MMAFM. All images were taken in tapping mode using TESP

silicon tips. The height images shown here are topographic maps of the surface with lighter colors representing upraised features and dark colors representing troughs.

Scanning electron microscopy was performed on a Hitachi Cold Field Emission SEM Model S-4500. It was not necessary to coat the samples with a conductive layer prior to imaging. Low beam voltages (6kV) were used to reduce charging effects.

X-ray photoelectron spectroscopy (XPS) was used to determine both the elemental composition and the chemical state of the surface. The strength of XPS for this study is that it can provide not only elemental composition but also oxidation state for several of the relevant oxides. It is also surface sensitive analyzing only the electrons that are sufficiently near the surface. The electron escape depth is element specific but a typical value is 1nm meaning that an electron 1nm below the surface has a probability of $1/e$ or $\sim 37\%$ of escaping the surface. XPS analysis were performed on a Physical Electronics 5400 ESCA system using Mg K alpha radiation (1253.6 eV) and a hemispherical analyzer pass energy of 17.90 eV giving an overall energy resolution of 1.0 eV. The spectra were charge corrected by referencing the binding energies to the C 1s photoelectron line arising from adventitious carbon at 284.6 eV.

3. Results

The potentiodynamic scans of Alloy 22 in SCW solution at 90C are shown in figure 1. The voltages are referenced with respect to an Ag/AgCl electrode (both here and throughout the paper). The two curves represent aerated and de-aerated conditions which can be seen to be quite similar. Due to these similarities, data is shown under both conditions interchangeably.

There are two constant current plateaus on the potentiodynamic curve. The first, at approximately 10^{-6} A/cm², is associated with passive film formation. The second plateau at approximately 10^{-4} A/cm² suggests that another stable oxide phase forms between 300mV and 600mV with respect to Ag/AgCl. Figure 2 shows atomic force microscopy images of the oxide films that were created by stopping the voltage scan when the current density is 10^{-6} A/cm² (passive region), 10^{-5} A/cm² (intermediate), and 10^{-4} A/cm² (second plateau), as indicated by the arrows in figure 1. All images have the same lateral scale (2 μ m x 2 μ m) however the z-scale is adjusted to give reasonable contrast and thus the smooth surfaces shown in figure 2a and figure 2b have smaller z-scales than the surfaces grown at higher polarizations.

The passive oxide film (figure 2b) is very smooth with a root mean square (RMS) roughness of 0.2 nm for the 2 μ m x 2 μ m image shown. A representative cross-sectional view of the oxide topography is shown below the image. The surface morphology and RMS roughness does not differ significantly from the polished and air-oxidized sample shown in figure 2a. It is likely that the oxide film is thicker after the potentiodynamic scan however the AFM probes relative surface variations not absolute thickness.

From image 2c, stopped midway between the plateaus, we begin to have some morphological indication that the oxide is growing. The surface has distinct domes and the RMS roughness has increased to 1.4 nm for the 2 μ m x 2 μ m image shown. The cross-sectional view shown below the image reflects this with a larger z-scale as compared to the passive film and a more regular pattern.

The most dramatic changes occur for scans stopped in the second plateau with current density near 10^{-4} A/cm². These surfaces have an open porous structure composed

of interconnected filaments. Surface roughness is now 40 times greater at 60nm for the 2 μ m image. From the cross-sectional view below the image, it can be seen that the pore openings are several hundred nanometers deep. From the AFM images the measured filaments widths are \sim 0.2 μ m. However, the interaction of the surface with the sides of the AFM tip broadens features (especially tall features) thus it is useful to also image using scanning electron microscopy (SEM) which does not broaden lateral features. From the SEM image in Figure 3, the filament widths are more accurately determined to be \sim 0.05-0.1 μ m.

Under sufficiently oxidizing conditions the metal can be driven into transpassive dissolution. Figure 4 shows a sample stopped in this region ($E \sim 800$ mV, $I \sim 6$ mA/cm²). The porous oxide overlayer is not well-adhered to the surface in this region and can be partially rinsed away under a stream of water. Figure 4a is an AFM image of a 10 μ m \times 10 μ m area where the porous oxide has partially delaminated exposing the underlying layer. A cross-section taken from near the center is shown below the image. The porous oxide is approximately 300nm thick. The underlying oxide is also dissolving at this stage and has a distribution of pits 50-100nm deep. It is worth enunciating that the AFM is much more sensitive to variations in height than most other imaging techniques. These "pits" would not be observed optically and are unlikely to be observed by SEM without signal averaging. Thus these pits are much shallower than pits usually referred to in corrosion literature.

Figure 5 shows an AFM image of a 20 μ m region where the porous oxide overlayer has been removed. The image is centered on the triple junction of three metal grains. Lines have been drawn as guides to the eye to show the grain boundaries. If the dissolution process were faster at the grain boundaries the image would show deep trenches outlining the grains rather than these barely discernable boundaries.

XPS Results:

Regions such as those shown in figure 4a provide an opportunity to compare the composition of the oxide layers in the porous region with that of the underlying layer. X-ray photoelectron spectroscopy (XPS) was used to obtain compositional information.

Spectra for the nickel, chromium, molybdenum, iron and carbon are shown in figure 4b-4f for both the porous overlayer (top trace) and the underlying layer (lower trace). The shapes of the high-resolution data were compared with literature libraries to determine which elements were in metallic and oxide forms. These findings are summarized in Table 3. We are in the process of obtaining oxide standards so that more quantitative curve fitting can be attempted.

In the layer closest to the base-metal, oxides from all of the major metal constituents of alloy 22 were observed with the exception of tungsten. The nickel peaks are consistent with NiO. It is likely that chromium is in the form of Cr₂O₃ and that there are two stoichiometries of molybdenum however these need further verification. In this underlying layer the weak elemental peaks are also seen for nickel, chromium, and molybdenum suggesting that the oxide is absent or very thin on parts of the oxide. It is reasonable to expect that the elemental contributions come from the pits.

In contrast, the porous overlayer is a nickel and iron oxide with almost no chromium or molybdenum. There is no evidence of major salt deposits on either layer.

Discussion/Conclusion:

To summarize, the potentiodynamic curves of Alloy 22 in SCW at 90C have two distinct constant current plateaus; one associated with passive oxide formation and the other associated with the formation of a porous oxide layer over a compact oxide closer to the base-metal. While the composition of the oxide closest to the base-metal is composed of nickel, chromium, molybdenum and iron, the porous oxide overlayer is composed of only nickel and iron. Although the compositional differences between the films can be accounted for by a mechanism that allows for preferential dissolution of chromium and molybdenum, random dissolution of select elements from a homogeneous film cannot create the ~1000nm scale patterns observed. Thus if the film is created by dissolution of Mo and Cr then the oxide must then rearrange, presumably by diffusive processes to grow the porous nickel and iron oxide structures.

Alternatively, it is possible that the porous structures form by dissolution followed by re-precipitation of the less soluble elements. If the metal/oxide destabilizes due to anodic driving forces then the bulk metal can begin to dissolve at weak points in the oxide. The less soluble nickel and iron may then re-precipitate onto the surface in the vicinity of the dissolving flux. The newly adsorbed oxide could then act as a coating to protect the surface neighboring the pit. Thus, making the local neighborhood of an existing dissolution event less susceptible to the nucleation of a new pit. In this way, the re-precipitation process can provide a feedback mechanism that can create patterns from stochastic dissolution events.

Acknowledgements

This work was performed under the auspices of the U.S. Department of Energy by the University of California, Lawrence Livermore National Laboratory under contract No. W-7405-Eng-48.

References

| Element | Min weight % (Except Ni balance) | Max weight % (Except Ni balance) |
|------------|-------------------------------------|-------------------------------------|
| Nickel | 63 | 50.025 |
| Chromium | 20 | 22.5 |
| Molybdenum | 12.5 | 14.5 |
| Iron | 2 | 6 |
| Tungsten | 2.5 | 3.5 |
| Cobalt | 0 | 2.5 |
| Carbon | 0 | 0.01 |
| Silicon | 0 | 0.08 |
| Manganese | 0 | 0.5 |
| Vanadium | 0 | 0.35 |
| Phosphorus | 0 | 0.025 |
| Sulfur | 0 | 0.01 |

Table 1: Constituents of nickel-based alloy 22 (UNS N06022).

| Element | mg/l |
|------------------|-------|
| K | 3330 |
| Na | 41370 |
| NO ₃ | 6410 |
| SO ₄ | 11550 |
| SiO ₃ | 130 |
| Cl | 6700 |
| Mg | 50 |
| Ca | 140 |
| F | 1440 |
| CO ₃ | 76150 |

Table 2: Simulated Concentrated Water (SCW) constituents.

| Element | Porous Overlayer | Underlying Layer |
|------------|---------------------------------------|--|
| Nickel | Oxide | Oxide and elemental |
| Chromium | Very little | Probably both oxide and elemental |
| Molybdenum | Very little | Elemental, two stoichiometries of oxide |
| Iron | Oxide | Oxide |
| Oxygen | Metal oxide, water (OH ⁻) | Metal oxide, more water (OH ⁻) than porous overlayer |
| Carbon | C=O C-C C-H | C=O C-O C-C C-H |

Table 3: Qualitative summary of XPS observations.

Figure Captions:

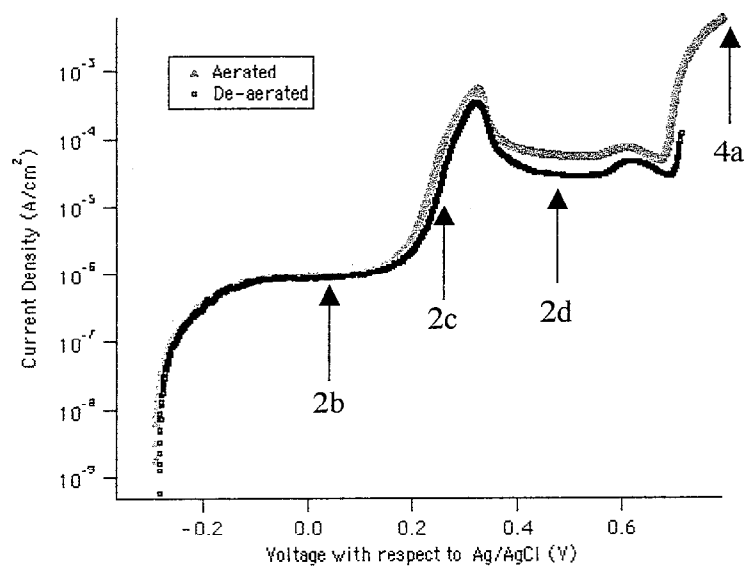
Figure 1: Current density versus Potential during a potentiodynamics scan of alloy 22 in 90 C SCW solution both under aerated (grey) and de-aerated (black) conditions. The potential is given in volts with respect to a cooled Ag/AgCl reference electrode. The current-voltage behavior from the open circuit potential to the transpassive dissolution region is very similar in these two cases. The arrows mark approximate positions where the potentiodynamic scans were stopped. The labels identify the images taken of these surfaces.

Figure 2: Atomic force microscope images of the oxide surfaces that form on alloy 22 when stopped at various points along a potentiodynamic scan (as indicated by the arrows in figure 1). All images show a $2\mu\text{m} \times 2\mu\text{m}$ area. Each has a different z-scale. a) Freshly polished initial substrate b) Scan stopped in the passive region. c) Scan stopped midway between the plateaus d) Scan stopped in the second plateau with a current density $\sim 10^{-4} \text{ A/cm}^2$.

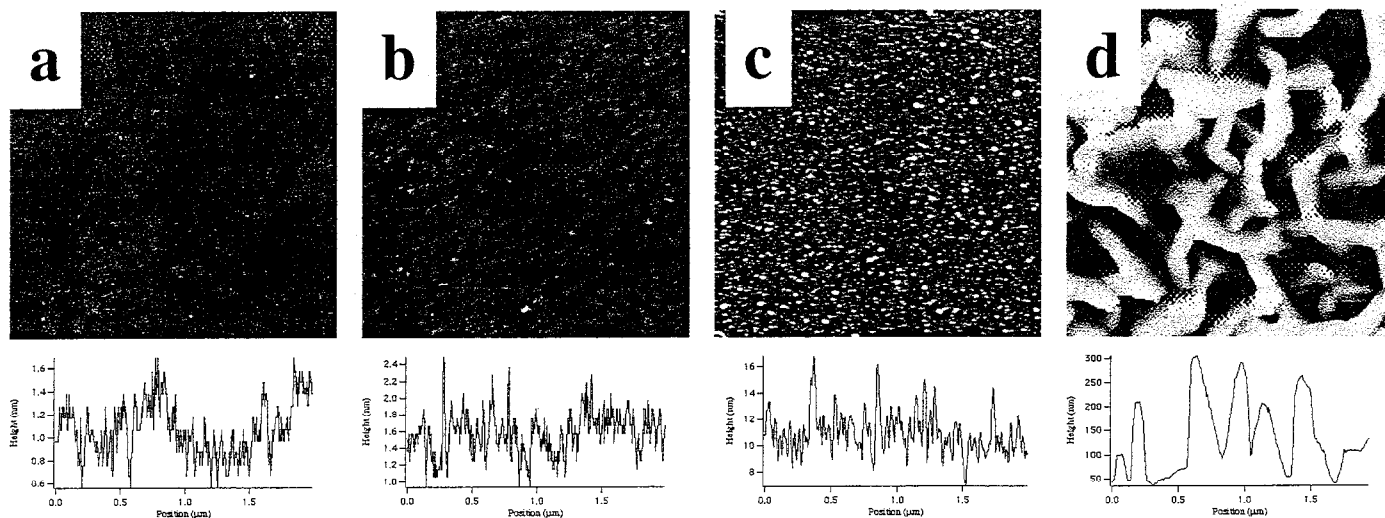
Figure 3: Scanning electron microscope image of porous oxide overlayer formed on alloy 22 in 90C SCW after anodic excursion. A relatively low electron beam voltage was used (6kV). From the SEM image the filament widths measure $\sim 0.05 \mu\text{m}$. A 1 micron scale bar is shown on the image.

Figure 4: Atomic force microscope image of a sample stopped while undergoing transpassive dissolution. Under these extreme oxidizing conditions and high currents the porous oxide overlayer begins to delaminate and is removed in patches when rinsing the sample in water. This provides an opportunity to compare the composition of both layers on the same sample. a) AFM image of a $10\mu\text{m} \times 10\mu\text{m}$ area. A cross-section (taken from near the center of the image) is shown below the image. b-f) XPS data for the porous oxide (top trace) and the oxide nearest the base metal (lower trace). The data are offset from one another to allow them to both be seen on the same graph. High-resolution windows centered around: b) nickel c) chromium, d) molybdenum, e) iron, and f) carbon. Both layers have nickel and iron but only the underlying layer has significant chromium and molybdenum. These data are summarized in table 3.

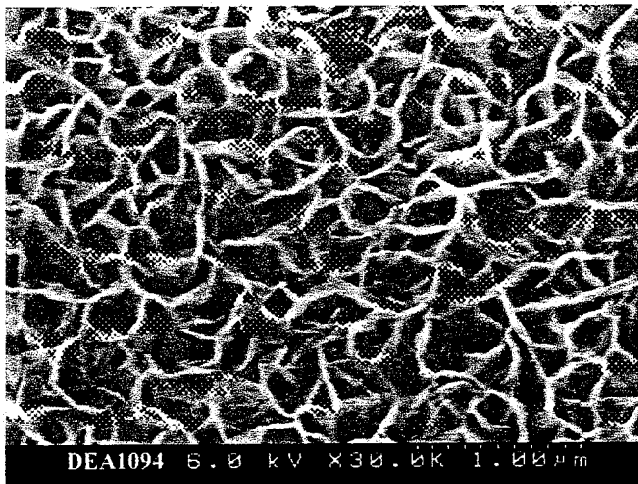
Figure 5: Atomic force microscope image of the sample shown in figure 4 which is stopped while undergoing transpassive dissolution. This image shows a $20\mu\text{m} \times 20\mu\text{m}$ area on the oxide nearest the metal at a triple junction of three metal grains. Lines have been drawn as guides to the eye to show the location of the barely visible grain boundaries. This image shows that dissolution is not preferential at the grain boundaries under these conditions.



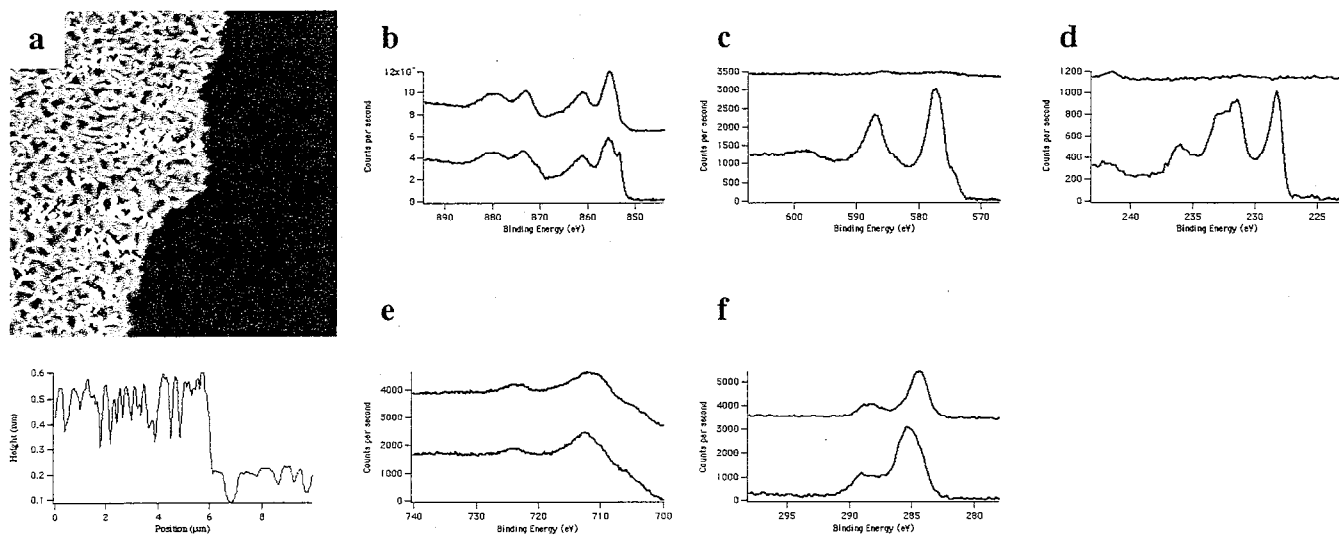
Figure



Figure



Figure



Figure

